

The Properties of Prestellar Discs in Isolated and Multiple Prestellar Systems

T. Hayfield^{1,2*}, L. Mayer³, J. Wadsley⁴, and A. C. Boley⁵

¹ *Institute of Astronomy, Physics Department, ETH Zürich, Wolfgang-Pauli-Strasse 27, CH–8093 Zürich, Switzerland*

² *Max-Planck-Institut für Astronomie, Königstuhl 17, D-69117 Heidelberg, Germany*

³ *Institute of Theoretical Physics, University of Zürich, Winterthurerstrasse 190, CH–8057 Zürich, Switzerland*

⁴ *Department of Physics & Astronomy, McMaster University, 1280 Main St. West, Hamilton ON L8S 4M1 Canada*

⁵ *Astronomy Department, University of Florida, 211 Bryant Space Science Center, PO Box 112055, USA*

Accepted . Received ; in original form .

ABSTRACT

We present high-resolution 3D smoothed particle hydrodynamics simulations of the formation and evolution of protostellar discs in a turbulent molecular cloud. Using a piecewise polytropic equation of state, we perform two sets of simulations. In both cases we find that isolated systems undergo a fundamentally different evolution than members of binary or multiple systems. When formed, isolated systems must accrete mass and increase their specific angular momentum, leading to the formation of massive, extended discs, which undergo strong gravitational instabilities and are susceptible to disc fragmentation. Fragments with initial masses of $5.5 M_{\text{jup}}$, $7.4 M_{\text{jup}}$ and $12 M_{\text{jup}}$ are produced in our simulations. In binaries and small clusters, we observe that due to competition for material from the parent core, members do not accrete significant amounts of high specific angular momentum gas relative to isolated systems. We find that discs in multiple systems are strongly self-gravitating but that they are stable against fragmentation due to disc truncation and mass profile steepening by tides, accretion of high specific angular momentum gas by other members, and angular momentum being redirected into members' orbits. In general, we expect disc fragmentation to be less likely in clusters and to be more a feature of isolated systems.

Key words: protostellar collapse – protostellar discs – gravitational instability

1 INTRODUCTION

The overall paradigm under which star formation occurs remains under debate. One hypothesis is that stars are thought to form as a collection of low mass fragments in collapsing clumps of gas, and then undergo competitive accretion as the fragments try to accrete gas from their common reservoir (Bonnell et al. 2001; Bonnell & Bate 2006). The main competing hypothesis is gravitational collapse, where massive star-forming clumps collapse and form multiple cores. Each star forms from the gas that is available in its own core, with limited accretion from other material in the parent clump (Krumholz et al. 2005). Regardless of the star formation paradigm, in the case of solar-type stars, the end result is most likely membership in a binary or multiple system (Duquennoy & Mayor 1991; Eggenberger et al. 2004). Scenarios for the formation of such systems abound. Amongst the simplest, most idealised scenarios are the fission of a bar-unstable core (Durisen et al. 1986; Burkert et al. 1997) and the fragmentation of centrally condensed, rotating, magnetised cores (Boss 1997a).

More complicated hypotheses appeal to the chaos of the cloud environment, such as core-core collisions (Turner et al. 1995), protostellar encounters (Shen et al. 2010), dynamical capture in unstable multiple systems (Bate et al. 2002), and accretion-triggered fragmentation (Bonnell 1994; Whitworth et al. 1995; Hennebelle et al. 2004; Offner et al. 2008; Kratter et al. 2010).

Star formation scenarios involving the rapid collapse of a protostellar core following the loss of support against gravity require the formation of a massive accretion disc around the central object (e.g. Vorobyov & Basu 2007 and Walch et al. 2009). Such discs undergo a short-lived ~ 0.1 Myr stage where the disc is massive relative to its host ($0.1 < M_d/M_* < 1$) and where gravitational instabilities operate to transport mass through the disc onto the central protostar (Vorobyov & Basu 2007). Massive, accreting, and extended protostellar discs have been shown to be susceptible to fragmentation, which could be responsible for a range of phenomena such as FU Orionis events and early dust processing if the clumps are disrupted (Boley et al. 2010; Nayakshin 2010), and the formation of substellar companions otherwise (Vorobyov & Basu 2007 and Boley 2009).

* hayfield@mpia.de

Given the problem that both the standard core accretion

planet formation timescale and protostellar disc lifetimes are typically a few Myr (Haisch et al. 2001), the idea of creating giant planets in a few orbital times via gravitational instabilities was revived (Boss 1997b) and has since been the subject of sustained interest (Boss 2002, 2008; Mayer et al. 2004, 2007; Pickett et al. 2000; Pickett & Durisen 2007; Boley et al. 2006; Boley 2009). Analytical works constraining inner disc fragmentation (Rafikov 2005, 2007), and the short cooling times required to form long-lived clumps within ~ 10 AU in simulations of protoplanetary discs, along with observations of massive planets on wide orbits (e.g. Marois et al. 2008, 2010), have led to a shift in focus to outer disc (> 40 AU) fragmentation (e.g. Stamatellos et al. 2007; Boley 2009; Dodson-Robinson et al. 2009; Vorobyov & Basu 2010). Whether the extended disc models used in these studies are similar to discs formed from collapsed molecular cloud cores remains to be seen.

In light of the likely connection between outer disc fragmentation and early protostellar systems, we examine in this paper the formation of discs in detail using 3D SPH simulations of core collapse in turbulent molecular clouds. In particular we compare the early evolution in mass, surface density, specific angular momentum, and disc stability between several different systems under near-identical conditions. In one set of simulations we compare an isolated and a binary system, and in the other we compare an isolated system and a small cluster. Previous studies of gravitational instabilities in binary systems have yielded mixed results, with some finding that the perturbing companion hinders fragmentation through disc truncation and tidal heating (Nelson 2000; Mayer et al. 2005) and alternatively promotes fragmentation, also through tidal perturbations (Boss 2006). However, the evolved systems considered in these studies may not be as susceptible to fragmentation as their protobinary counterparts, which we investigate here, due to the enhanced importance of gravitational instabilities during protostellar disc formation.

The paper is laid out as follows: in Section 2 we discuss the simulations, initial conditions and the clump identification procedure. In Section 3 we present the results and analysis. Further discussion is provided in Section 4, and our conclusions are laid out in Section 5.

2 THE SIMULATIONS

All calculations were run with Gasoline (Wadsley et al. 2004), a parallel implementation of TreeSPH. We employ a fixed number N of smoothing neighbors, with the main runs using $N = 32$. Artificial viscosity is the standard prescription (Gingold & Monaghan 1983) with $\alpha = 1$, $\beta = 2$, controlled with a Balsara switch (Balsara 1989).

2.1 Initial Conditions

The cloud in this experiment is spherical and uniform with a radius of 0.188 pc, a mass of $50 M_{\odot}$, and a temperature of 10 K, as in Bate et al. 2003. It was seeded with supersonic turbulent velocities and is marginally self-bound. To simulate interstellar turbulence, the velocity field of the cloud was generated on a grid as a divergence-free Gaussian random field with an imposed power spectrum $P(k) \propto k^{-4}$. The resulting velocity dispersion $\sigma(l)$ varies as $l^{1/2}$, and is consistent with the Larson scaling relations (Larson 1981). The velocities were then interpolated from the grid to the particles. Finally, the condition that the cloud be

marginally self-bound gives a normalization for the global velocity dispersion of 1.17 km s^{-1} . We describe the results of two simulations in this paper, run A and run B. Runs A & B are different random realizations of the same ICs, with the same power spectrum, but with different initial phases of the velocity field. As a result the first objects that form in run A (which are the only ones that we can follow owing to the high computational expense of modeling hydrodynamics at high resolution without employing sinks), are different from those in run B. In run A we have two sub-simulations, one in which a binary system naturally arises, and another in which we suppress the production of the secondary. We then compare the subsequent evolution of the systems in an otherwise identical core and cloud environment. In run B an isolated system and a cluster are produced roughly coevally at opposing ends of a filamentary structure. We compare the evolution in these systems, having been produced in similar environments.

2.1.1 Run A: The Isolated and Binary Systems

We describe here how we produced the isolated system in run A. The fiducial cloud free fall time is given by $t_{\text{ff}} = \sqrt{3\pi/32G\rho_{cl}} = 1.92 \times 10^5 \text{ yr}$, with $\rho_{cl} = 1.2 \times 10^{-19} \text{ g cc}^{-1}$ being the initial cloud density. The evolution of the cloud was followed up to $t = 1.2 t_{\text{ff}}$.

At $t = 0.88 t_{\text{ff}}$ a core, whose collapse we follow in detail, has already formed a small central protostar. The protostar accretes rapidly via a connecting filament until the filament itself produces a fragment. The fragment survives first pericenter with the protostar and becomes a companion.

We produced an isolated system for comparison under near-identical conditions by tracing the particles comprising the companion back in time to $t = 0.88 t_{\text{ff}}$ and stirring them by randomly exchanging their velocities. This procedure conserves the energy and linear momentum but not the angular momentum of the stirred particles. There were approximately 5300 particles, totaling $0.053 M_{\odot}$, that had their velocities perturbed.

2.2 Thermodynamics

We model the thermodynamics of collapse with a piecewise polytropic equation of state (Tohline 1982 and Bate 1998):

$$P = \begin{cases} \kappa_0 \rho & \rho < 10^{-13}, \\ \kappa_1 \rho^{7/5} & 10^{-13} \leq \rho, \end{cases} \quad (1)$$

with κ_0 chosen so that the sound speed $c_s = 1.84 \times 10^4 \text{ cm s}^{-1}$ and the subsequent κ_1 chosen to ensure pressure continuity. Theoretical estimates of temperatures in molecular clouds find that their temperatures should range between 5–10 K over densities ranging from 10^{-19} – $10^{-13} \text{ g cc}^{-1}$ (Larson 1985; Low & Lynden-Bell 1976; Masunaga & Inutsuka 2000). Observations indicate a somewhat higher minimum temperature of 8 K, with typical temperatures of 10–13 K (Kirk et al. 2007). The equation of state thus captures the approximately isothermal behaviour of the cloud in the intermediate density regime. At high densities the gas transitions to being adiabatic with exponent $\gamma = 7/5$. This equation of state is a simplification of the internal heating and cooling processes in a molecular cloud and, in the high density regime, will minimize the potential for fragmentation. Furthermore, through our choice of softening ($\epsilon_g = 2.3 \text{ AU}$) combined with the polytropic equation of state, we allow the first hydrostatic core to be marginally resolved, while still inhibiting its subsequent dissociating collapse (Larson 1969), which can be computationally demand-

ing to resolve. Three-dimensional collapse simulations with more sophisticated thermodynamics, and including radiative transfer, but of isolated cores with no turbulent cloud environment, have been performed by (Whitehouse & Bate 2006; Bate 2010; Tomida et al. 2010; Commerçon et al. 2010). While proper treatments of both thermodynamics and radiative transfer are important, such simulations are computationally expensive and so far can only be carried out at lower resolution, and with shorter integration times than required in our calculations. We shall explore the problem with more detailed thermodynamics and radiative transfer in a future publication. We reiterate, though, that the early evolution of protostellar discs and protobinaries is still not understood. Before the complexities of radiation hydrodynamics can be introduced, the birth of these systems must be understood through examination of high-resolution hydrodynamics simulations with a reasonable, albeit simplified, EOS, which is the focus of this paper.

2.3 Resolution

The simulations employ 5 M particles. The particle masses m_p are thus $1.0 \times 10^{-5} M_\odot$ in all simulations. The minimum jeans mass M_j , defined as $M_j = 2.92 c_s^3 / (G^{3/2} \rho_0^{1/2})$, is that obtained at the transition density to the adiabatic equation of state, and is $M_j^* = 1.7 \times 10^{-3} M_\odot = 1.8 M_{j\text{up}}$. Previous work has shown that molecular clouds should have a minimum jeans mass (Low & Lynden-Bell 1976), with the gas becoming optically thick to its own cooling radiation at $\sim 10^{-13} \text{ g cc}^{-1}$. In our 5 M particle runs $M_j^*/m_p = 167$ and the jeans mass remains adequately resolved at all times. A fixed gravitational softening $\epsilon_g = 2.3 \text{ AU}$ is used in all simulations.

2.4 Disc Identification

In order to compare and separate the systems in the simulations, a working definition of what comprises a protostellar system is required. We define a protostellar system within this context as being a self-bound gas structure with a peak density greater than $6.7 \times 10^{-12} \text{ g cc}^{-1}$. The density threshold was chosen to be well above the critical density in order to identify only bound structures that are in the adiabatic regime. To determine whether any cold, isothermal gas is bound to a given system, we require that it is bound below a threshold binding energy $E_b = 2.6 \times 10^{34} \text{ erg}$. The binding energy criterion is imposed in order to exclude particles that are only marginally or not uniquely bound to the system, e.g., lying in the protostellar envelope or flowing between the primary and secondary. The value was chosen empirically to be as small as possible while minimising noise in the results.

To put this into practice we use the SKID (Stadel 2001) group finder. SKID works by pushing tracer particles along density gradients to find local maxima, and linking them with friends-of-friends. Once group assignments are found we then remove unbound particles to create self-bound groups, computing:

$$E = \frac{m_p}{2} |\mathbf{v} - \mathbf{v}_{cm}|^2 + U + E_{th} \quad (2)$$

as the total energy, with \mathbf{v} and \mathbf{v}_{cm} the velocity and center of mass velocity, U the gravitational potential, and E_{th} the thermal energy. The center of mass frame is updated throughout the unbinding procedure.

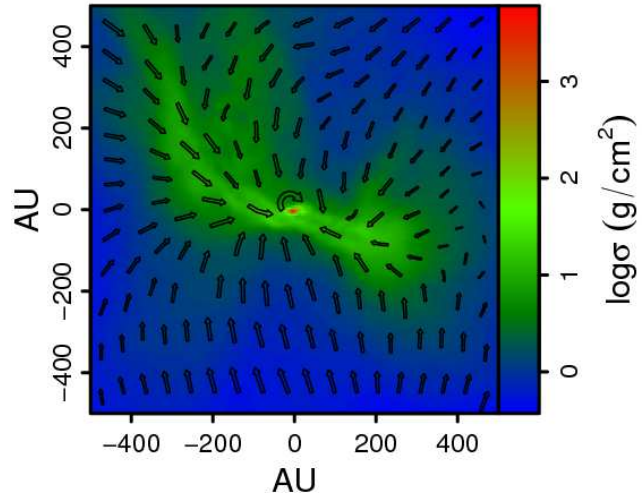


Figure 1. The column density and velocity field in a $(1000 \text{ AU})^3$ volume, containing $0.29 M_\odot$ of gas, around the central prestellar object. The time is $t = 0.88t_{\text{ff}}$, at the onset of core collapse.

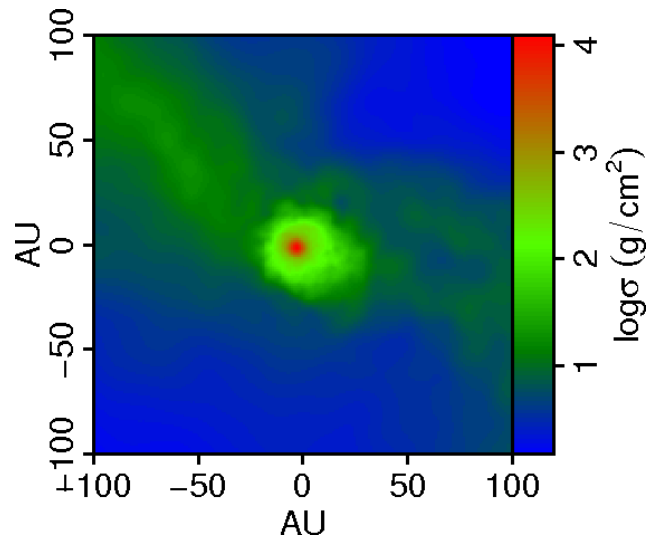


Figure 2. The protostellar object formed at the onset of its parental core's collapse at $t = 0.88t_{\text{ff}}$. The object is 1.7 kyr old at this stage with a disc of 25 AU in radius, and a mass of $0.055 M_\odot$.

3 Run A: RESULTS

At $t = 0.88t_{\text{ff}}$ a nascent protostellar system has begun to form from the collapse of its enveloping core. In Fig. 1, the surface density and velocity field, projected through a $(1000 \text{ AU})^3$ box cut around the prestellar object, are shown. The box contains $0.29 M_\odot$ of gas. The central prestellar object formed via fragmentation of a filament 1000 AU in extent. We see in the integrated transverse velocity field that accretion primarily occurs along the filament, as there is only a small torus of opening angles around the system from which low density material is observed to make a direct approach. Most gas collides with the filament and is subsequently funneled onto the system.

In Fig. 2, the surface density of the prestellar system, in projection along its axis of rotation, is shown. The system is $0.055 M_\odot$ and the disc is 25 AU. The filaments feeding the disc at this stage

have densities ranging from $7 \times 10^{-15} \text{ g cc}^{-1}$ up to the critical adiabatic density $10^{-13} \text{ g cc}^{-1}$. The system accretes rapidly until $t = 0.893t_{\text{ff}}$ whereupon a fragment of mass $8 \times 10^{-3} M_{\odot}$ forms in the low density filamentary material, close to the Jeans mass of $6.4 \times 10^{-3} M_{\odot}$. The fragment survives first pericenter and becomes a companion. The isolated system, in contrast, continued accreting material rapidly, building up the disc around the protostellar system.

3.1 Surface densities and temperatures

3.1.1 Surface Density Maps

In this section, we compare the divergent evolution of the isolated and binary systems. To accommodate the change in dynamical times at disc scales we set the units to kyr and count time relative to the formation of the system at $0.88t_{\text{ff}}$. In Fig. 3 we see the surface density maps of the isolated and the binary systems in the left and right columns respectively, shown at times 4.4 kyr, 5.8 kyr, and 7.1 kyr after formation of the primary (or equivalently, the isolated system). Differences appear early between the two systems. In the topmost row, we see that the primary in the binary system is similar to the isolated system in morphology and surface density except for a tidal disturbance of the disc caused by an initial close passage of the secondary. In the central row the differences are more pronounced. At 5.8 kyr we see that the isolated system has continued to grow in mass and the disc now has a radius of 50 AU. Between 4.4 kyr and 5.8 kyr approximately 1 orbital time has passed in the binary system and the secondary is at its apogee. The primary has shrunk in extent as the secondary has accreted some the gas in its outer regions. The secondary is also rapidly accreting high specific angular momentum gas from the two filaments feeding the system. In the bottom row at 7.1 kyr we see that the isolated system has continued to grow in mass and extent but has become gravitationally unstable and an $m = 2$ spiral arm has developed into a material arm. At 7.1 kyr the binary system has completed another orbit, both systems have grown in mass, and the same pattern of tidal disturbance of the primary is observed.

3.1.2 Temperature Maps

In Fig. 4, mass-weighted temperature maps of the binary and isolated systems, at times 4.4 kyr, 5.8 kyr and 7.1 kyr, are plotted, as in Fig. 3. As we are using a piecewise polytropic equation of state (Equation 1), some of the gas bound at the outer edge of the system(s) and some interarm gas is still in the isothermal phase. In the isolated system, increasing amounts of mass end up at large radii and at low densities, due to its higher specific angular momentum j (see section 3.2 for elaboration on these points). In the binary system however, pictured in the right column of Fig. 4, almost all of the mass identified as bound to each system lies at high densities (and is thus adiabatic) and within their respective tidal radii.

3.2 Disc Evolution

3.2.1 Disc Mass

In Fig. 5, the accretion histories of the isolated system, primary, and secondary are plotted. The mass at a given time is determined by the procedure outlined in 2.4, and is thus the combined protostellar and disc mass. The isolated system accretes gas steadily and at a high rate throughout the simulation, with typical accretion rates of

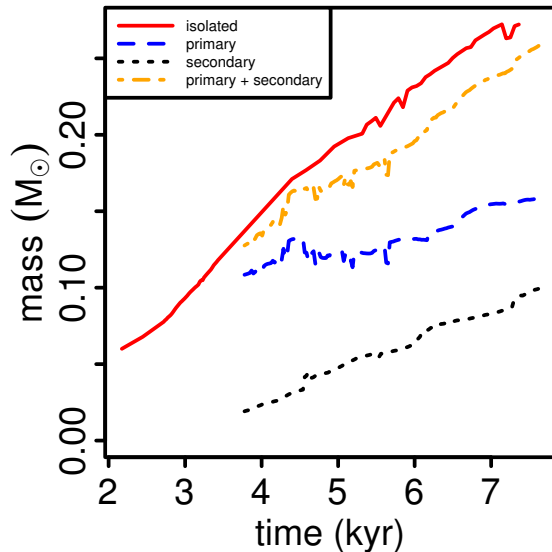


Figure 5. Total mass accreted (disc + protostar) versus time for the isolated, primary, and secondary systems, and the net mass in the binary system.

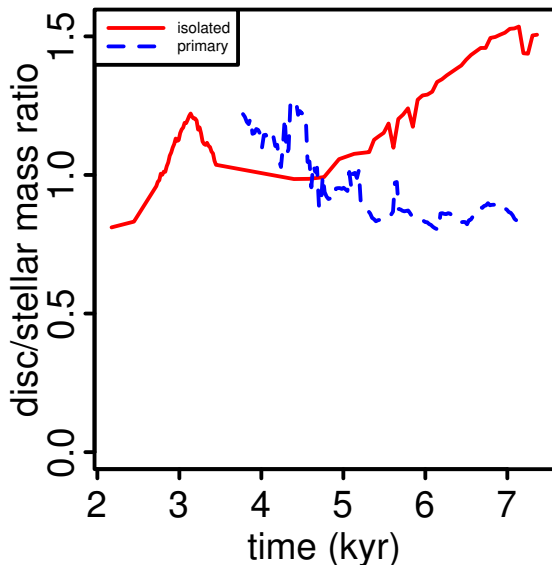


Figure 6. The ratio of disc mass to accreted stellar mass versus time, for the isolated, primary systems.

$3 - 5 \times 10^{-5} M_{\odot} \text{ yr}^{-1}$. After the initial collapse, the central protostar, defined as the mass contained within $r < 5 \text{ AU} \simeq 2\epsilon$, has an accretion rate of $5 - 6 \times 10^{-6} M_{\odot} \text{ yr}^{-1}$. Taking the asymptotic rate from 1D protostellar collapse theory, $\dot{M} = m_{\odot} \dot{c}_s^3 / G$ (Stahler & Palla 2005), we find that $\dot{M} = 2 \times 10^{-6} M_{\odot} \text{ yr}^{-1}$, and so m_{\odot} , a constant of order unity, is approximately 2.5 at the protostar. This is not a high accretion rate, as 1D collapse simulations asymptote to $m_{\odot} = 2$ (Stahler & Palla 2005). The accretion rate onto the entire system however, is high, with $m_{\odot} \sim 10$, and is perhaps due to embedding within a filament. Both accretion rates are

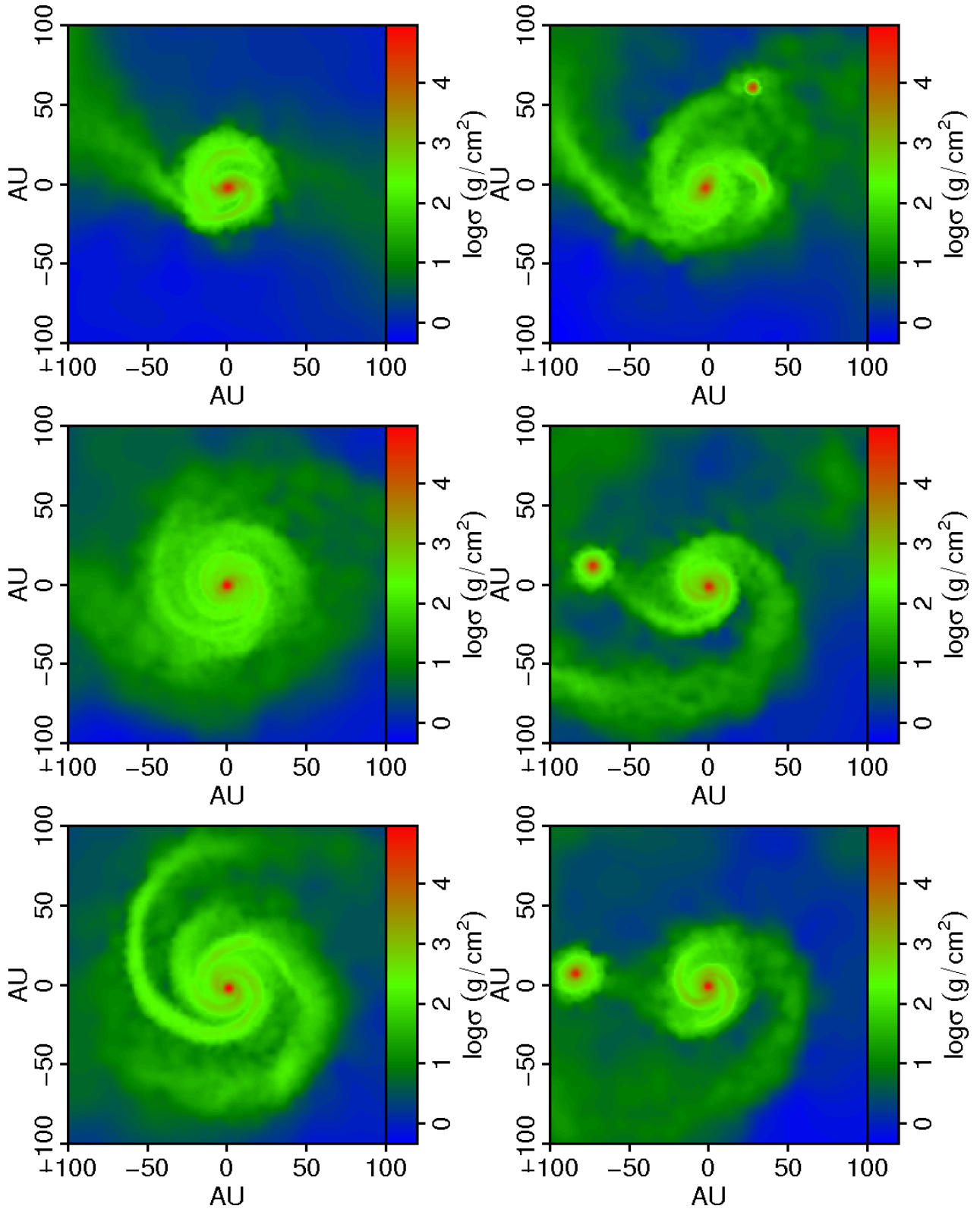


Figure 3. The surface densities of the isolated and binary systems, respectively in the left and right columns, and shown at times 4.4 kyr, 5.8 kyr, and 7.1 kyr from the top row to bottom, after formation.

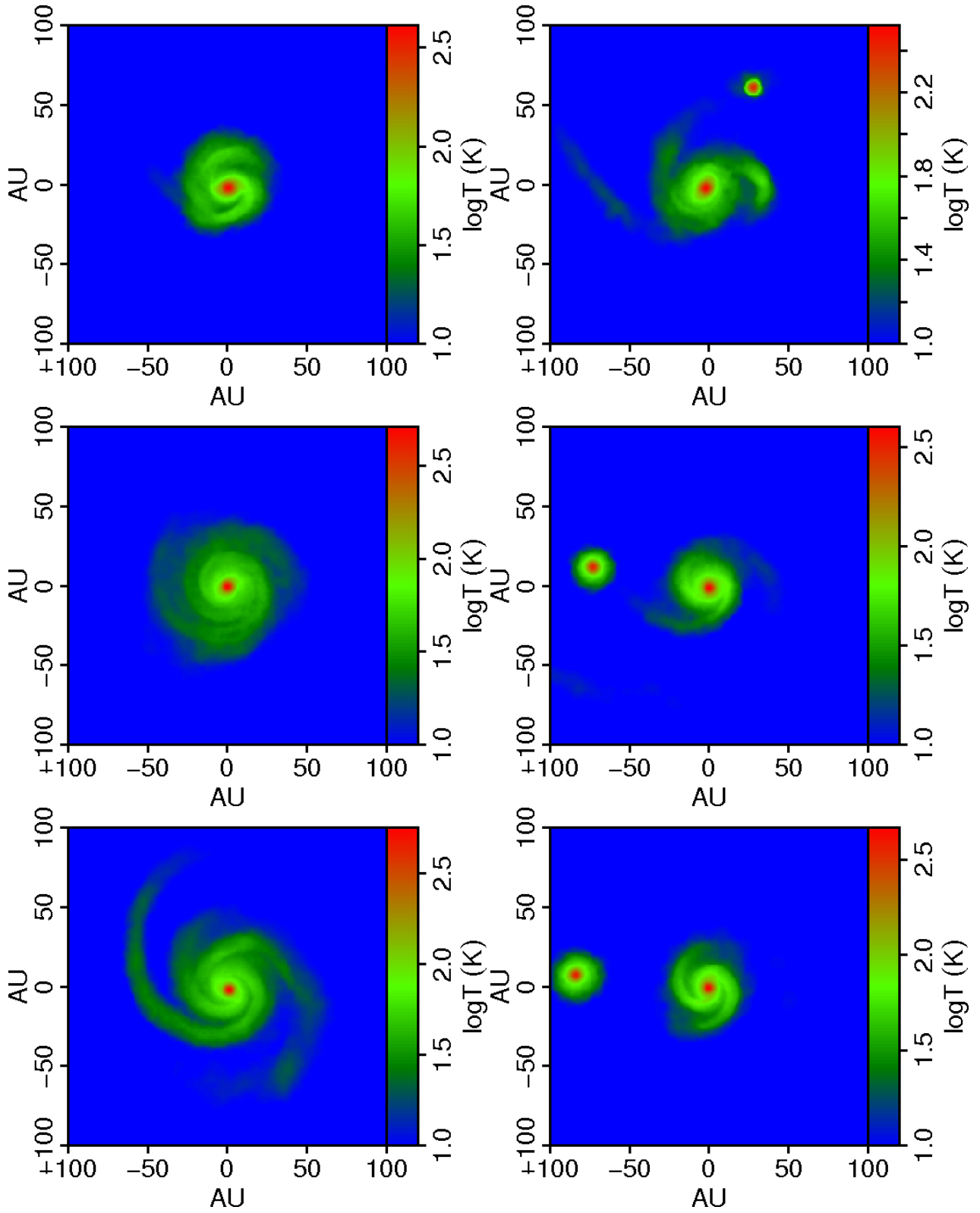


Figure 4. Mass-weighted temperature maps of the isolated and binary systems, respectively in the left and right columns, and shown at times 4.4 kyr, 5.8 kyr, and 7.1 kyr from the top row to bottom, after formation.

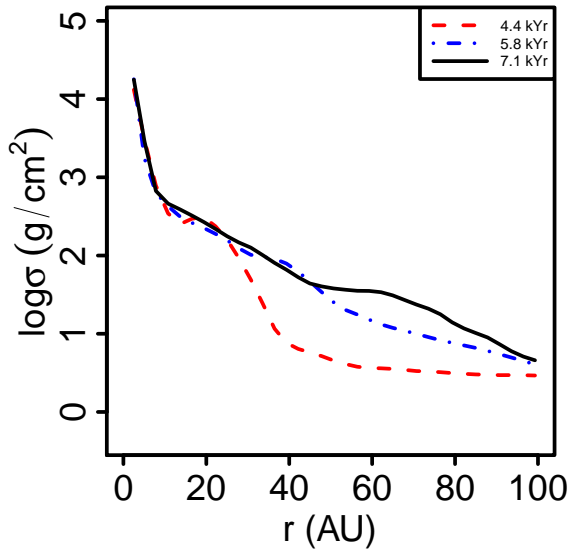


Figure 7. Evolution of the surface density profile of the isolated system. σ tends to increase at all radii with time.

consistent with other studies, such as those found in Walch et al. 2009.

As expected, the net mass accreted by the binary system is close to that of the isolated one. The difference between the two is because there is some mass present in the binary that can not be uniquely assigned either to the primary or secondary. The binary system is plotted starting at 3.8 kyr, instead of its formation time at 3330 yr, because during the first pericenter the identification procedure has difficulties separating the two objects uniquely. In the binary system the secondary, due to its orbit, preferentially accretes high specific angular momentum gas from the filaments and accretes mass at a higher rate than the primary, and at later times the mass ratio tends toward unity. This behaviour has been noted before in the literature (e.g. Bate & Bonnell 1997).

In Fig. 6, the ratio of stellar mass (the mass within 5 AU, chosen to correspond with the limits of our softening) to disc mass for the isolated and primary systems are plotted. The isolated system continues gaining disc mass faster than it can be transported to the star, while the primary evolves steadily towards stability. As systems normally become moderately self-gravitating at a mass ratio of ~ 0.1 , we see that these newly formed protostellar systems are in a regime dominated by gravitational instability.

3.2.2 Cumulative Mass Fraction and Mass Profiles

The discs in both the isolated and binary systems are all massive relative to the central protostar and exhibit strong spiral arms as seen in Figs. 3. We expect that tidal torques will, in addition, play a role in triggering mass transport within the discs in the binary as noted for example in (Mayer et al. 2005). In Figs. 7 & 8 are plotted the surface densities averaged in annuli of the isolated disc and of the primary of the binary system. We see from Fig. 7 that in the isolated system the trend as time progresses is toward increasing amounts of mass at all radii, while from Fig. 9 it is evident that the relative amount of mass at large radii is increasing, illustrated by the outward movement of the half-mass radius. The surface density profile of the primary in the binary system (see

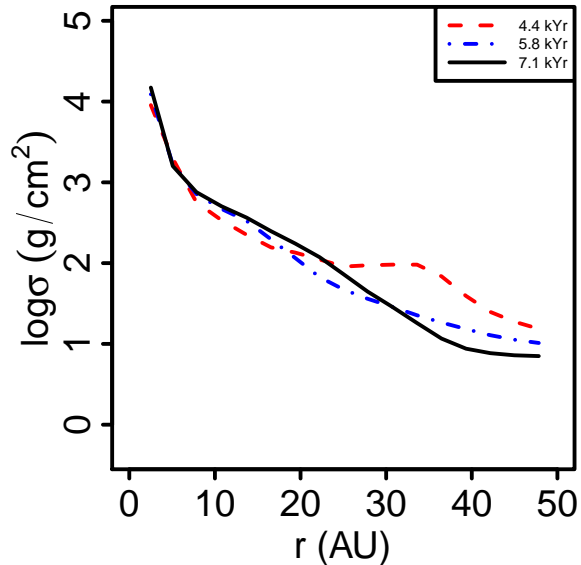


Figure 8. Evolution of the surface density profile of the primary in the binary system. σ decreases steadily at outer radii and increases at inner radii due to tidal interactions.

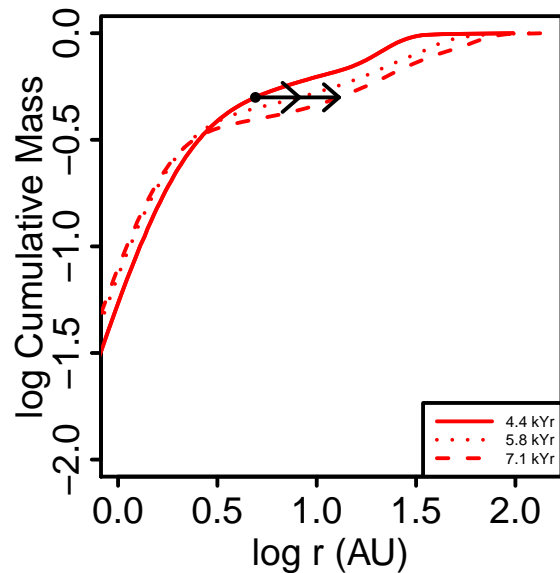


Figure 9. The mass profile evolution of the isolated system. As time progresses, increasing amounts of mass relative to the total lies at large radii. We illustrate this by plotting the evolution of the half-mass radius in black.

Fig. 8) shows increasing surface density within 20 AU and clearly decreasing surface density outside of 30 AU throughout the simulation. This is reflected in the cumulative mass profile in fig. 10 as a decreasing overall fraction of mass found at larger radii, and the clear inward movement of the half-mass radius (while the total mass slowly increases). The source of this difference is likely increased mass transport from gravitationally amplified tidal perturbations. To illustrate the role of tidal effects we model the primary and secondary as point masses and compute the Jacobi radius r_j at

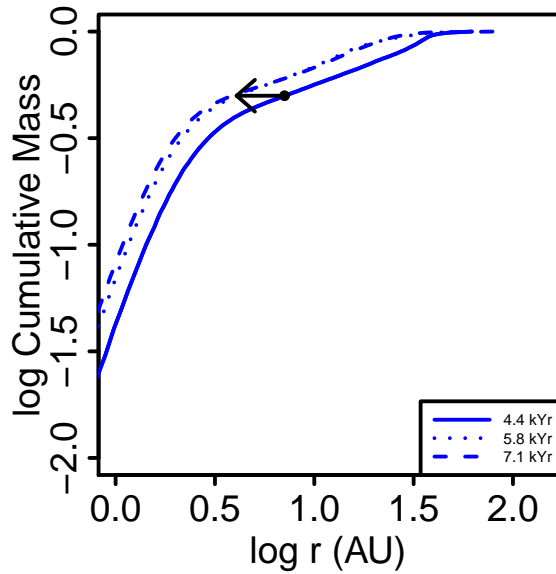


Figure 10. The mass profile evolution of primary. In contrast to Fig. 9 we see the relative fraction of mass at large radii decreasing with time. We illustrate this by plotting the evolution of the half-mass radius in black.

5.8 kyr given the nominal values $M = 0.125 M_{\odot}$, $m = 0.05 M_{\odot}$ and $R_0 = 75$ AU (see Figs. 5 & 3) for the primary mass, secondary mass and separation, respectively. Given these parameters we compute $r_j = 0.41R_0 = 31$ AU, thus we expect tidal effects to, at the very least, limit the disc of the primary to 44 AU. Looking at the cumulative mass profile, we see that at our disc-finding procedure is roughly consistent with such a simple model, with very little bound mass found outside of 30 AU.

3.2.3 Temperature Profiles

In Figs. 11 & 12 are plotted the temperature profiles in the isolated and binary systems, respectively. At times 4.4 kyr and 5.8 kyr, the temperature declines steadily from 250 K to 10 K at 40 AU and ~ 60 AU respectively, whereupon it remains at the temperature floor for larger radii, however there is little mass at these radii (see Fig. 9). At time 7.1 kyr, the disc becomes more extended, and the temperature profile flattens at large radii. The disk contains a mixture of isothermal and adiabatic gas, with the spiral arms containing most of the adiabatic component. In the binary system (Fig. 12), the temperature profiles of the primary lack the low temperature, low density component seen in the isolated system due to truncation of the disc at the tidal radius, and do not evolve much after 5.8 kyr.

3.2.4 Specific Angular Momentum

In Fig. 13 are plotted the combined disc and protostellar specific angular momenta for the isolated system, primary and secondary. Each measure is computed in the centre-of-mass frame of the given systems and is thus a measure of the spin (i.e. disc) component of the specific angular momentum. The isolated system rapidly increases in specific angular momentum, and after 7.1 kyr, becomes unstable to fragmentation. In the binary system the primary has a small spike in its specific angular momentum j at 4.2 kyr due to weakly bound material appearing to be bound to the primary while

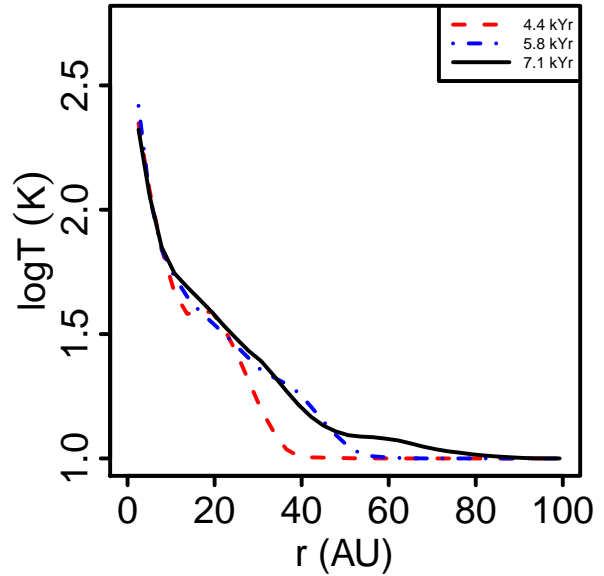


Figure 11. Azimuthally mass-averaged temperatures in the isolated system. At later times the high j gas has formed an extended disc which includes cold interarm gas around the primary, leading to a break in the temperature profile.

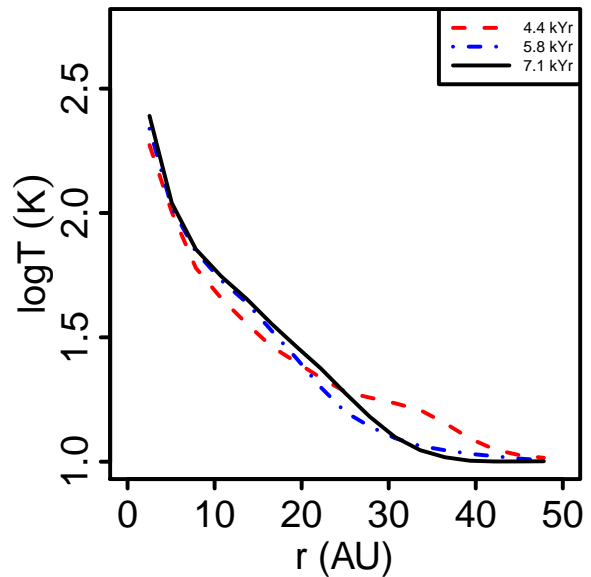


Figure 12. Azimuthally mass-averaged temperatures in the primary of the binary system. The disc remains limited by tidal forces, and almost all bound gas is adiabatic.

the secondary reaches pericenter. This is also seen in the mass plot at the same time. The primary exhibits very little evolution in j thereafter, while from Fig. 5 we see that it continues to accrete mass in the interim; it accretes at constant j . In contrast the secondary increases steadily in j along with M .

Part of the reason that the binary increases more slowly in specific angular momentum than the isolated system, is that it is able to store momentum in the binary orbit. To measure this effect,

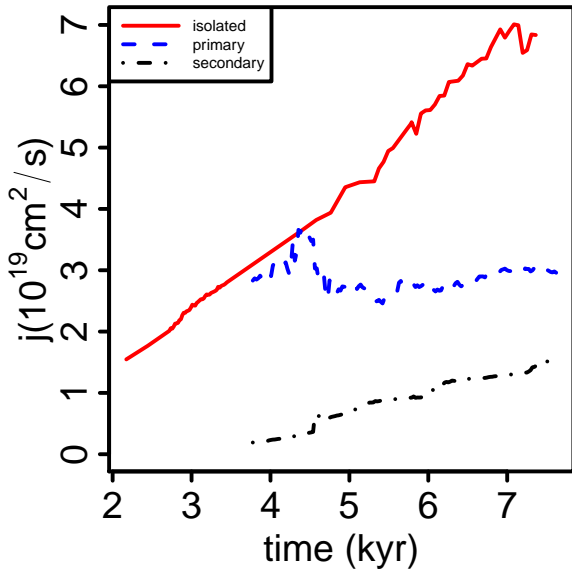


Figure 13. Evolution of the specific angular momentum j of the isolated and binary systems. j grows rapidly for the isolated system and leads to a more rapid buildup of an extended disc, whereas tidal effects and lower j leads to smaller discs in the binary system.

we use the relationship

$$\mathbf{L} = \sum_i \mathbf{R}_i \times \mathbf{P}_i = \mathbf{R} \times \mathbf{P} + \sum_i \mathbf{r}_i \times \mathbf{p}_i \quad (3)$$

where \mathbf{L} is the angular momentum, \mathbf{R}_i are the positions of each particle, \mathbf{P}_i are the particle momenta, \mathbf{R} is the barycentre, \mathbf{P} the velocity of the barycentre, \mathbf{r}_i and \mathbf{p}_i positions and momenta relative to the barycentric frame, and decompose the binary into spin and centre of mass angular momenta. We further get the specific angular momentum using the appropriate mass-weightings along with Equation 3. At $t = 7.1$ kyr, we find that in the barycentric frame, the isolated system has a specific angular momentum of $7.0 \times 10^{19} \text{ cm}^2 \text{ s}^{-1}$. In the binary system, the binary orbit itself has $6.1 \times 10^{19} \text{ cm}^2 \text{ s}^{-1}$, the primary has $3.0 \times 10^{19} \text{ cm}^2 \text{ s}^{-1}$ and the secondary $1.3 \times 10^{19} \text{ cm}^2 \text{ s}^{-1}$ (also visible from Fig. 13). The specific angular momentum of the binary orbit dominates that found in the other components.

We quantify alignment of the specific angular momentum of the disc with that of the environment by computing the angle $\theta = \cos^{-1}(\hat{\mathbf{j}}_d \cdot \hat{\mathbf{j}}_e)$, with $\hat{\mathbf{j}}_d$ being the unit vector of the specific angular momentum of the disc and $\hat{\mathbf{j}}_e$ being that of the material in the environment in a box of dimensions 2000^3 AU^3 surrounding the system. At the time of formation of the system (Figs. 1 & 2) we find $\theta = 36^\circ$. In the isolated system we observe angles of 13° , 7.7° , 12° at times 4.4 kyr, 5.8 kyr and 7.1 kyr, respectively. In the binary system the $\hat{\mathbf{j}}_d$ of the primary is 18° , 7.3° , 5.3° at times 4.4 kyr, 5.8 kyr and 7.1 kyr. The vectors tend to be oriented perpendicular to the major axes of the filaments feeding the disc. Such relatively small misalignments are consistent with other works suggesting filaments tumbling about one of their shorter axes as the origin of protostellar angular momentum (Walch et al. 2009) and with observations of protostellar systems on these length scales, which find that most gas is extended in the direction perpendicular to outflows (Tobin et al. 2010).

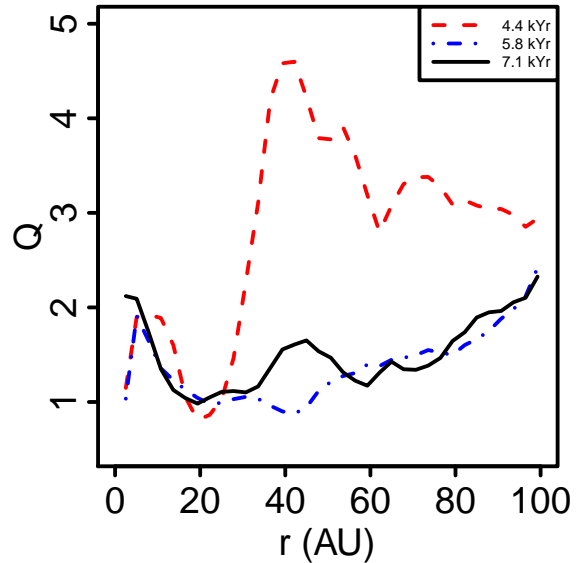


Figure 14. Azimuthally averaged Toomre Q for the isolated system at times 4.4 kyr, 5.8 kyr and 7.1 kyr.

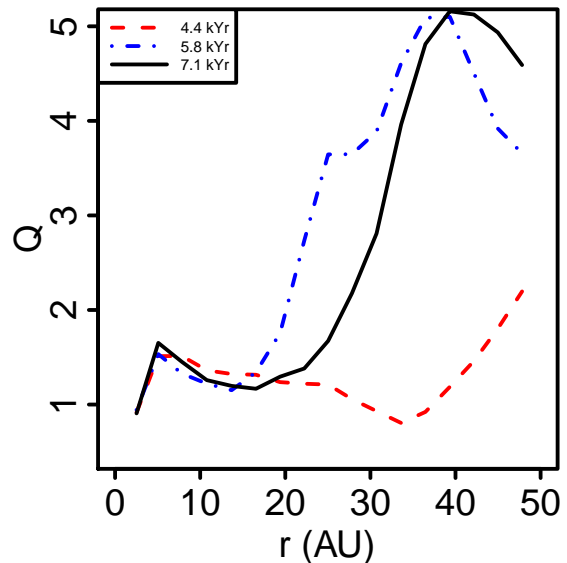


Figure 15. Azimuthally averaged Toomre Q for the binary system at times 4.4 kyr, 5.8 kyr and 7.1 kyr. The binary system remains stable for as long as the simulation was run (20 kyr).

3.3 Stability and Fragmentation

Throughout the simulation(s), the discs of both the isolated and binary systems are massive and gravitationally unstable. To compare stability we compute the Toomre $Q = c_s \kappa / \pi G \sigma$ parameter locally using mass-weighted projections, through a $200 \times 200 \times 200 \text{ AU}^3$ box, followed by azimuthal averages, of the disc. The results are shown in Figs. 14 & 15. Although the Q curve for the isolated system drops below unity in some regions at 4.4 kyr it does not fragment right away. As the envelope is accreted, the disc evolves

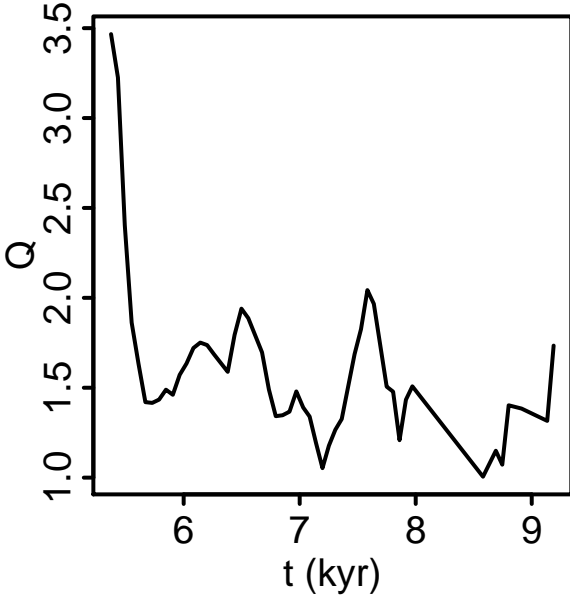


Figure 16. Toomre Q parameter of the isolated system averaged in an annulus from 60–70 AU in times preceding clump formation. A clump later forms at 9.2 kyr at 65 AU.

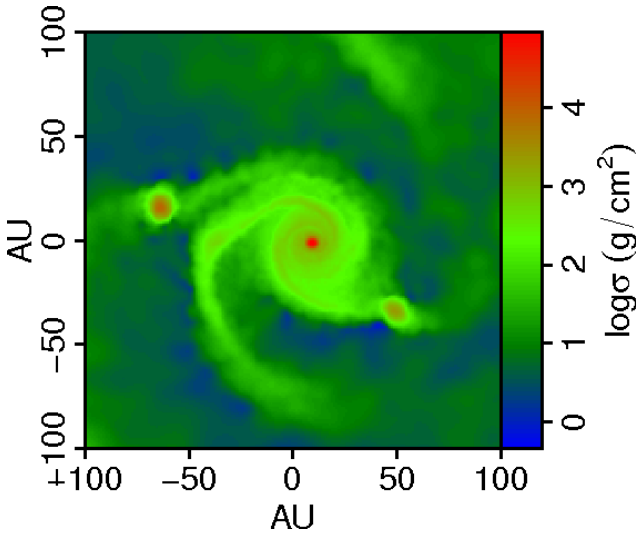


Figure 17. A surface density map of the isolated system at $t = 11$ kyr, approximately one orbital time after the second fragment formed.

to a state where Q lies between one and two out to 90 AU. The disk remains in the unstable regime, but Q varies substantially as the system accretes. In contrast, the primary of the binary system has a minimum Q of 1.3 at later times and, except initially, rises above two at radii greater than 25 AU. The binary system is thus significantly more stable than the isolated one, and this is borne out by the fact that it does not fragment at later times (up to 20 kyr).

At 9.2 kyr we find that the isolated system becomes unstable to fragmentation, forming two clumps, one at $r = 65$ AU, followed by another at $r = 100$ AU in the disc. The first clump (C1) formed in one of the material arms of the disc from adiabatic gas, with an initial mass of $5.5 M_{\text{jup}}$ and specific angular momentum of $1.8 \times 10^{18} \text{ cm}^2 \text{ s}^{-1}$. The second clump (C2) formed at

10 kyr, had a mass of $7.4 M_{\text{jup}}$ and specific angular momentum of $3.2 \times 10^{18} \text{ cm}^2 \text{ s}^{-1}$. We seek to understand formation of the first clump from adiabatic gas by looking at the behavior of Q in the run-up to fragmentation. In Fig. 16 is plotted the Q parameter averaged in an annulus ranging from 60–70 AU. Q starts off initially very high but drops as continuing accretion builds up the disc in this region. Both clumps are depicted in Fig. 17 at 11 kyr. At this time, clump C1 has made approximately 1.5 orbits and has a mass of $39 M_{\text{jup}}$, and clump C2 one half-orbit, has grown to $14 M_{\text{jup}}$. Both clumps accrete at a rate of roughly $10^{-5} M_{\odot} \text{ yr}^{-1}$.

4 Run B: RESULTS

We describe here the results from a complimentary simulation, run B. At approximately $t = 1.1 t_{\text{ff}}$ fragments form at either end of a long (7400 AU) filament, within ~ 2 kyr of each other. In the following discussion and figures, we set $t = 1.1 t_{\text{ff}}$ as being $t = 0$, as it is at this time when the first system, the isolated system, forms.

The upper left image in Fig. 18 is a surface density plot of the filament, projected through a $(10^4 \text{ AU})^3$ box. At the top end of the filament lies the isolated system and the cluster is located at the bottom. The upper right image in Fig. 18 is the surface density of the cluster at the end of simulation. Only three of four members are shown. The two systems in the upper left corner of the image have formed a binary, in the sense that they complete orbits around their centre of mass on a time scale shorter than the cluster crossing time. For a more complete discussion of the cluster evolution, see 4.1.

In the second and third rows of Fig. 18, are the surface densities and mass-weighted temperature maps of the isolated system (lying at the top of the filament), at 4.3 kyr, and 8.7 kyr. In the isolated system we see the disc assemble rapidly from infalling filamentary gas, going through stages of increasing gravitational instability, until, as shown in the bottom row of Fig. 18, gas trailing at the end of one of the material arms in the disc fragments. As seen in the temperature maps, the gas in the fragment was in the adiabatic regime. The initial clump mass is $12 M_{\text{jup}}$.

4.1 Cluster Evolution

In Fig. 4.1 are plotted the distances of cluster members to the origin of a fiducial cluster frame vs. time. Since the cluster is a rapidly evolving object at this stage, we choose the fiducial frame as being the one which moves in a straight line from the original position of the first clump to its final position. We can see in Fig. 4.1 that members are typically ~ 100 AU from the origin in this frame. Members spend most of their time in binary associations, whereby it is meant that they orbit around their common center of mass on timescales shorter than the cluster crossing time. Two such binaries can be seen at points A and B in Fig. 4.1, through the mutual oscillation of their distances in the cluster frame. At point C in the figure, the members of the cluster converge briefly and their mutual separations become comparable to their binary separations. Between C and D, a merger occurs, and a new binary forms, with the remaining member being sent on a larger orbit.

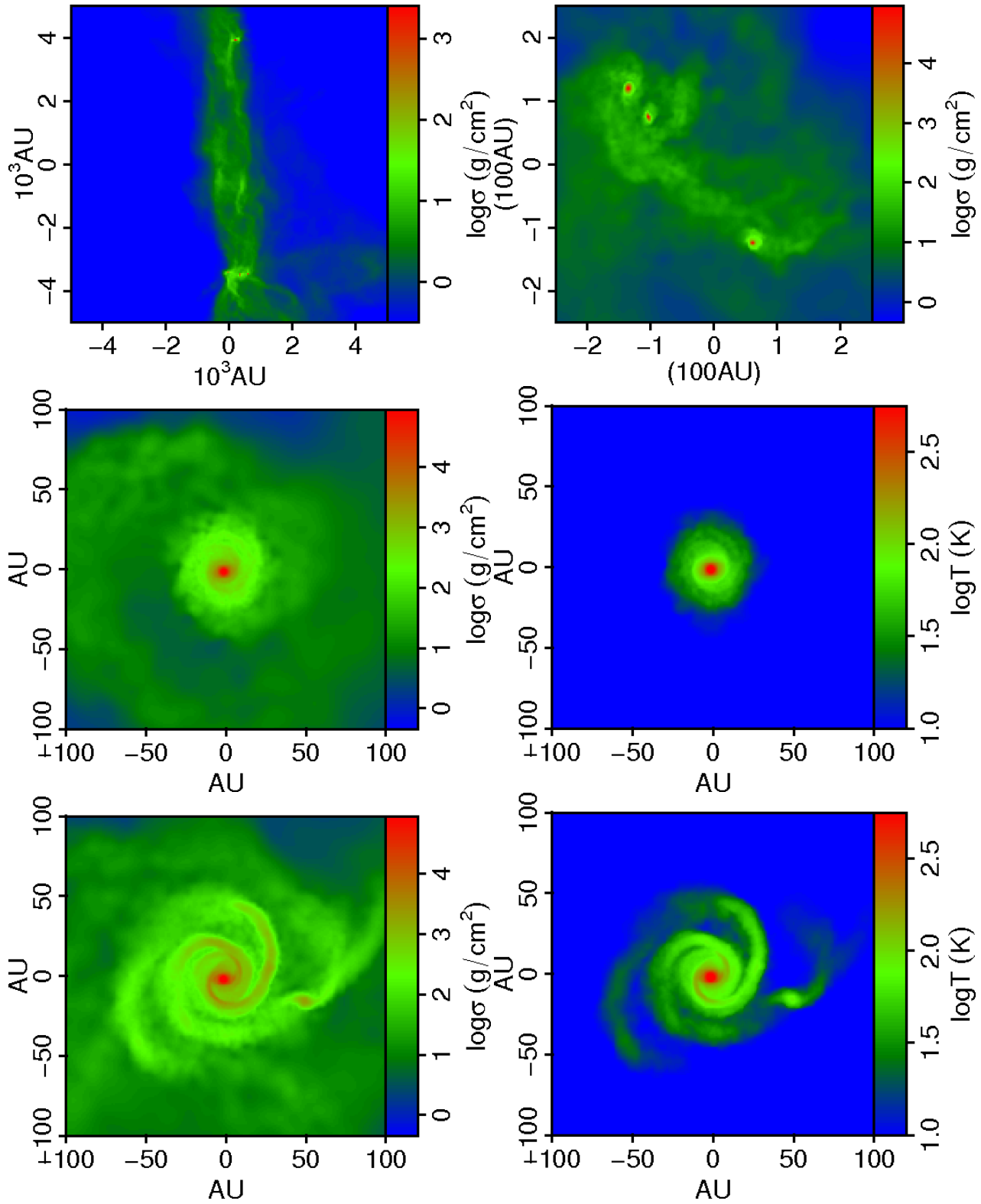


Figure 18. First row, Left: Surface density map of filament formed in run B. At the top and bottom of the filament are the isolated system and cluster, respectively. Right: The cluster as seen at the end of the simulation. One member, 10^3 AU away, is not shown. Second and third rows: The surface densities and mass-weighted temperature maps of the isolated system, respectively in the left and right columns, shown at times 4.3 kyr, and 8.7 kyr, after formation.

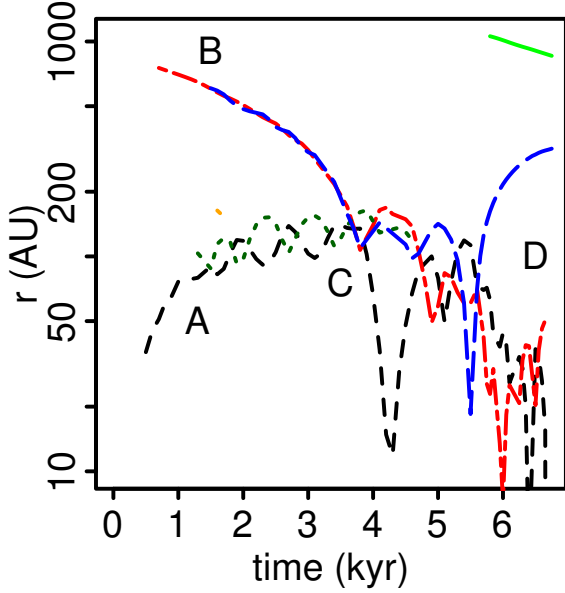


Figure 19. Distance from the origin of a fiducial cluster frame of reference vs. time, for various members of the cluster. The frame of reference is based on the trajectory of the oldest member, hence the separation approaches zero at the beginning and end of the data. Several objects pair up to form short lived 'binaries' while in the cluster. Two such binaries can be seen at points A and B in Fig. 4.1, through the mutual oscillation of their distances in the cluster frame. At point C, all extant members of the cluster briefly converge. Between C and D, a merger occurs, leading to the formation of a new binary and the ejection of the third member.

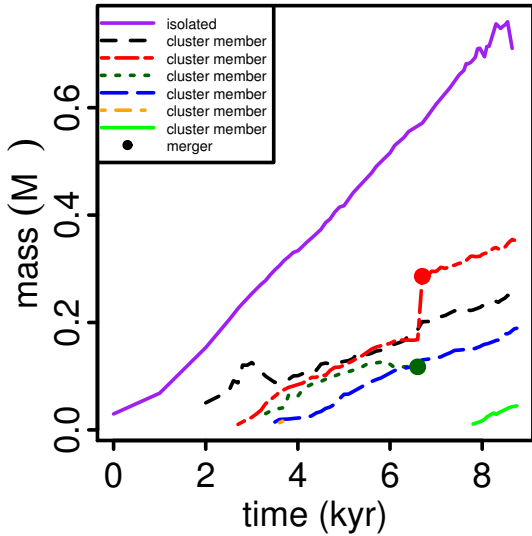


Figure 20. Total mass accreted (disc + protostar) versus time for the isolated system, and the cluster. A merger occurs between two prestellar systems in the cluster at 6.3 kyr.

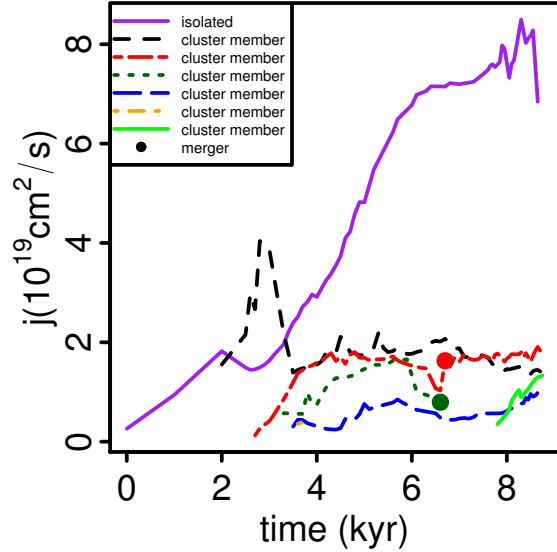


Figure 21. Evolution of the specific angular momentum j of the isolated system and the cluster. j grows rapidly for the isolated system and leads to a more rapid buildup of an extended disc, whereas various tidal effects and close encounters lower j and leads to smaller discs in the binary system.

4.2 Disc Evolution

4.2.1 Disc Mass

In Fig. 20, the accretion histories of the isolated system, and those of all objects formed in the cluster are plotted. The isolated system accretes gas at a high rate, at an average of $8 \times 10^{-5} M_{\odot} \text{ yr}^{-1}$. The accretion rates observed are quite comparable to those for the isolated system from run A, and thus they are well above the expected asymptotic rates ($m_{\circ} \gtrsim 10$).

For the cluster, the average accretion rate is $\sim 3 \times 10^{-5} M_{\odot} \text{ yr}^{-1}$, with little deviation between objects. The evolution of the cluster is complex. The pattern of fragmentation of core gas never yielded objects which were isolated for very long, quickly leading to the production of a couple of short-lived binaries with similar evolution (similar accretion rates and generally limited disc size). A major merger occurs at 6.3 kyr; the result of a head-on collision between two clumps. Given the chaos of the cluster, the accretion rates as seen by the slopes in Fig. 20 are remarkably uniform.

4.2.2 Specific Angular Momentum

In Fig. 21 are plotted the combined disc and protostellar specific angular momenta for the isolated system, and for the objects in the cluster. As in run A, the isolated system rapidly increases in specific angular momentum. Upon reaching $\sim 7 \times 10^{19} \text{ cm}^2 \text{ s}^{-1}$, material arms form in the isolated system, moving angular momentum out of the system, and allowing angular momentum to remain constant while accretion continues (compare to Fig. 20). As the arms become stronger, the determination of j becomes more difficult, because gas is ejected with increasing violence from the ends of the material arms back into the envelope. About 1 kyr after the onset of this behaviour, the arm fragments (shown in Fig. 18).

The evolution of the cluster angular momenta shows a rather remarkable contrast. Following Fig. 21 once more, we see that the

first object to form in the cluster evolves as one might expect, with both mass and specific angular momentum increasing. Once other fragments form in the cluster, the specific angular momentum of the system drops until hitting a maximum value which appears to characterise the entire cluster. The pattern of fragmentation in the core never left any object in the cluster truly isolated for very long, with some short-lived binaries forming, sometimes ending in mergers, but generally lasting long enough to tidally limit and alter the structure of the discs of cluster members. Referring once more to the mass evolution plots in Fig.20, we see that accretion continues, somewhat abated by the competition amongst cluster members for infalling gas. We see then a stronger, clearer, reiteration of the result from run A, namely that upon hitting a threshold, accretion continues but at constant specific angular momentum.

The major merger occurring at 6.3 kyr, indicated by the large filled circles in Fig. 21 has an interesting effect on the angular momenta of the merging systems. Their momenta both dip quite suddenly at the time of collision. This is due to the ejection of plumes of high- j gas at the moment of merger. The gas is then quickly accreted onto the new system, bringing it back up to the angular momentum ceiling for the cluster.

5 DISCUSSION

5.1 Fragmentation

5.1.1 Accretion and specific angular momentum

In the simulations performed the isolated systems become prone to fragmentation via the development of massive material arms, even though the gas is adiabatic. Instabilities in the isolated systems are driven by steady accretion of gas with increasing specific angular momentum. The disc, sufficiently massive to generate spiral arms, accumulates a reservoir of gas lying at large radii (i.e. with high specific angular momentum). This reservoir is then swept up by the spiral arms, which when sufficiently massive, become prone to fragmentation; such instabilities have been documented in similar contexts in the literature (e.g. Bonnell 1994; Whitworth et al. 1995; Hennebelle et al. 2004). At the same time, Offner et al. (2008) observe that in simulations of freely decaying turbulence the resulting protostellar systems are more prone to fragmentation, and attribute it to high rates of accretion. Seeing as the isolated systems in the present study have accretion rates several times that of the nominal 1D asymptotic rate, perhaps the tendency toward fragmentation observed by Offner et al. (2008) is due to a combination of higher accretion rates and accretion of gas with high specific momentum. Furthermore, it could be that the continued driving of turbulence is reducing the specific angular momentum of accreted gas, or acting as a viscosity and depleting the reservoirs of gas which would otherwise be swept up in dense material arms.

The binary system from run A and the systems in the cluster from run B remain stable throughout the simulation. Although the discs are sufficiently massive to be self-gravitating, and the systems are accreting, a number of effects work against outer disc fragmentation. The tidal limiting of the discs, as discussed in section 3.2.2, is a major barrier to fragmentation. In run A, although the binary separation evolves (increases) throughout the simulation, by the end of our run the separation is ~ 75 AU, and given the tendency of the binary mass ratio to approach unity (e.g. Bate & Bonnell 1997), there is very little chance for outer disc fragmentation to occur. In run B the cluster appeared to have an effective ceiling in the specific angular momentum for member systems. Longer simulations

looking at the long term evolution of multiple systems and clusters should be undertaken to see if they separate sufficiently to allow extended discs to grow. Even if at some later point they do grow, fragmentation is less likely because most mass will likely have made it onto the star and a high disc/star mass ratio will be harder to achieve, also, accretion rates decrease as time progresses. In run A, the tendency for the secondary to accrete high specific angular momentum gas as seen in this paper and in other studies of binaries (e.g. Bate & Bonnell 1997), acts strongly to deplete the reservoir of gas in the outer part of the system and shuts out the possibility for the growth of the same Toomre instability which lead to fragmentation of the isolated system. Furthermore, the enhanced inward transport of mass due to tidal torques shown in 3.2.2 acts to stabilise the disc against fragmentation, an effect that has also been observed by (e.g. Mayer et al. 2005).

5.1.2 Accretion and gas temperatures

In the following we discuss analyse run A in more detail. In the isolated system two clumps form by the end of the simulation. They form in the outer reaches of the disc where temperatures were low, and where some interarm gas is still isothermal at 10 K, although clump C1 forms in a material arm from adiabatic gas with a temperature of ~ 30 K. Recent simulations of star formation including a flux-limited diffusion treatment for radiative transfer and some modelling of protostellar accretion emphasise the importance of radiative feedback on the envelope. To estimate the effect we compute the accretion luminosity of the protostar (Stahler & Palla 2005):

$$\begin{aligned} L_{acc} &= \frac{GM_*\dot{M}}{R_*} \\ &= 61 L_{\odot} \left(\frac{\dot{M}}{10^{-5} M_{\odot} \text{ yr}^{-1}} \right) \left(\frac{M_*}{1 M_{\odot}} \right) \left(\frac{R_*}{5 R_{\odot}} \right)^{-1} \quad (4) \end{aligned}$$

with $M_* = 0.11 M_{\odot}$ being the protostellar mass, which we compute by taking all mass within $r \leq 5 \text{ AU} \simeq 2\epsilon$; $\dot{M} = 5 \times 10^{-6} M_{\odot} \text{ yr}^{-1}$ is the (time-averaged) accretion rate onto the protostar, and R_* the protostellar radius that, since it is sub-grid, we assume a fiducial value of $5 R_{\odot}$. From this we get a typical accretion luminosity of $L_{acc} = 3.4 L_{\odot}$. Clump C1 forms at $r_c = 65 \text{ AU}$. To try to get an upper limit on the temperature at that radius, we assume that the disc presents an absorbing surface of height $h = 10 \text{ AU}$ spanning $r_c \pm 5 \text{ AU}$, and that all of the accretion luminosity crossing this surface deposits all of its energy in this region, yielding a heating rate of $L_{acc}h/2r_c = 10^{33} \text{ erg s}^{-1}$. We assume D'Alessio et al. (2001) opacities and a $1 \mu\text{m}$ grain size, and a background irradiation temperature of 30 K, and using the existing density field of the gas within $r_c \pm 5 \text{ AU}$ at the time of fragmentation, we calculate the temperature at which the cooling rate balances the heating rate of the gas to be 50 K. We wish to emphasise that the assumptions made here are extremely conservative with the aim of bracketing the upper end of conceivable outer disc temperatures. Given the weak dependence of Q on T , it does not appear that the accretion luminosity will be able to affect the disc stability at these large radii.

5.1.3 Clump masses and accretion rates

Again, we limit the discussion here to run A for brevity. The isolated system forms two clumps of masses $5.5 M_{\text{jup}}$ and $7.4 M_{\text{jup}}$. What kind of clump masses should one expect in the outer disc?

Because the disc is in a disordered state at the time of clump formation we do not compare the clump masses to those computed from axisymmetric models, but instead we compute the local Jeans mass of the clump-forming gas, which for clump C1 was $4.7 M_{\text{Jup}}$, and that of clump C2 was $4.5 M_{\text{Jup}}$. The particle mass in the simulations was $10^{-5} M_{\odot}$, hence in the clumps the Jeans mass is resolved with ~ 450 particles, or ~ 14 smoothing kernels. The fragmentation phenomena are thus well-resolved according to the criteria set forth in the literature (Bate & Burkert 1997; Nelson 2006). In addition, the initial angular momentum radii of the clumps are 0.31 AU and 0.73 AU, respectively, and should they undergo a second collapse in $\sim 10^4$ years due to H_2 dissociation, any accretion onto the final body will take place through an accretion disc (Boley et al. 2010). We observe final clump masses of $39 M_{\text{Jup}}$ and $14 M_{\text{Jup}}$ for C1 and C2, respectively, however whether or not dissociative collapse will occur before these masses are achieved is highly sensitive to assumptions about the dust. We emphasise here that the connection between our final obtained clumps and the substellar companions (the planets or brown dwarfs) produced from them is uncertain. A dissociating collapse of the clumps and the establishment of an accretion disc is a certainty, however other dynamical instabilities may form, such as a bar instability, and can play a role in redistributing mass and angular momentum. Because the simulation lacks the necessary physics and resolution to follow the internal evolution of the clumps, we refrain from speculating on the final object masses. Nevertheless, we can estimate accretion luminosities for our final clumps using our clump parameters. Both clumps C1 and C2 had accretion rates of $\sim 10^{-5} M_{\odot} \text{yr}^{-1}$. Computing the accretion luminosity using Equation 4, inputting the measured accretion rate, clump masses of $5.5\text{--}39 M_{\odot}$, and assuming a fiducial final size of $1 R_{\text{Jup}} = 7 \times 10^9 \text{ cm}$, gives accretion luminosities ranging between $16\text{--}110 L_{\odot}$. Such relatively high luminosities are achieved at this accretion rate because the radius of Jupiter is ~ 50 times smaller than our fiducial one for the central protostar ($5 R_{\odot}$). With such extremely high luminosities we can see that mass accretion simply cannot continue unabated without feedback playing some role. Our final clump masses and luminosities thus fall on the upper end of the range of expected values.

6 CONCLUSIONS

The primary motivation of this paper was to compare the evolution of an isolated and binary/multiple systems during the early stages of prestellar development within the same environment. Of particular interest was the potential for fragmentation of such early, accreting and self-gravitating discs. The following are our findings:

- The initial collapse occurs within filaments that tend to colimate infalling gas onto the central prestellar objects, whose specific angular momenta tend to remain aligned to that of the environment (and perpendicular to the embedding filament) on scales of $\sim 1000 \text{ AU}$.

- During formation, isolated systems must accrete mass and increase their specific angular momentum, leading to the formation of massive, extended discs, which undergo strong gravitational instabilities and are susceptible to fragmentation

- In systems starting out as binaries and multiples, an effective specific angular momentum ceiling exists, limiting the maximum j of the systems but not their mass, making disc fragmentation unlikely. The ceiling is the product of tidal interactions which strip cold gas from members, and concentrate their mass profiles, and the redirection of angular momentum into orbits.

7 ACKNOWLEDGEMENTS

The computations were performed in part on the Brutus cluster at the ETH Zürich, and the zBox2 and zBox3 supercomputers at the ITP, University of Zürich.

REFERENCES

- Balsara D. S., 1989, PhD thesis, , Univ. Illinois at Urbana-Champaign, (1989)
- Bate M. R., 1998, *ApJ*, 508, L95
- Bate M. R., 2010, *MNRAS*, 404, L79
- Bate M. R., Bonnell I. A., 1997, *MNRAS*, 285, 33
- Bate M. R., Bonnell I. A., Bromm V., 2002, *MNRAS*, 336, 705
- Bate M. R., Bonnell I. A., Bromm V., 2003, *MNRAS*, 339, 577
- Bate M. R., Burkert A., 1997, *MNRAS*, 288, 1060
- Boley A. C., 2009, *ApJ*, 695, L53
- Boley A. C., Hayfield T., Mayer L., Durisen R. H., 2010, *Icarus*, in press
- Boley A. C., Mejía A. C., Durisen R. H., Cai K., Pickett M. K., D’Alessio P., 2006, *ApJ*, 651, 517
- Bonnell I. A., 1994, *MNRAS*, 269, 837
- Bonnell I. A., Bate M. R., 2006, *MNRAS*, 370, 488
- Bonnell I. A., Bate M. R., Clarke C. J., Pringle J. E., 2001, *MNRAS*, 323, 785
- Boss A. P., 1997a, *ApJ*, 483, 309
- Boss A. P., 1997b, *Science*, 276, 1836
- Boss A. P., 2002, *ApJ*, 576, 462
- Boss A. P., 2006, *ApJ*, 641, 1148
- Boss A. P., 2008, *ApJ*, 677, 607
- Burkert A., Bate M. R., Bodenheimer P., 1997, *MNRAS*, 289, 497
- Commerçon B., Hennebelle P., Audit E., Chabrier G., Teyssier R., 2010, *A&A*, 510, L3+
- D’Alessio P., Calvet N., Hartmann L., 2001, *ApJ*, 553, 321
- Dodson-Robinson S. E., Veras D., Ford E. B., Beichman C. A., 2009, *ApJ*, 707, 79
- Duquennoy A., Mayor M., 1991, *A&A*, 248, 485
- Durisen R. H., Gingold R. A., Tohline J. E., Boss A. P., 1986, *ApJ*, 305, 281
- Eggenberger A., Udry S., Mayor M., 2004, *A&A*, 417, 353
- Gingold R. A., Monaghan J. J., 1983, *MNRAS*, 204, 715
- Haisch Jr. K. E., Lada E. A., Lada C. J., 2001, *ApJ*, 553, L153
- Hennebelle P., Whitworth A. P., Cha S., Goodwin S. P., 2004, *MNRAS*, 348, 687
- Kirk J. M., Ward-Thompson D., André P., 2007, *MNRAS*, 375, 843
- Kratter K. M., Murray-Clay R. A., Youdin A. N., 2010, *ApJ*, 710, 1375
- Krumholz M. R., McKee C. F., Klein R. I., 2005, *Nature*, 438, 332
- Larson R. B., 1969, *MNRAS*, 145, 271
- Larson R. B., 1981, *MNRAS*, 194, 809
- Larson R. B., 1985, *MNRAS*, 214, 379
- Low C., Lynden-Bell D., 1976, *MNRAS*, 176, 367
- Marois C., Macintosh B., Barman T., Zuckerman B., Song I., Patience J., Lafrenière D., Doyon R., 2008, *Science*, 322, 1348
- Marois C., Zuckerman B., Konopacky Q. M., Macintosh B., Barman T., 2010, *Nature*, 468, 1080
- Masunaga H., Inutsuka S., 2000, *ApJ*, 531, 350
- Mayer L., Lufkin G., Quinn T., Wadsley J., 2007, *ApJ*, 661, L77
- Mayer L., Quinn T., Wadsley J., Stadel J., 2004, *ApJ*, 609, 1045
- Mayer L., Wadsley J., Quinn T., Stadel J., 2005, *MNRAS*, 363, 641

- Nayakshin S., 2010, MNRAS, 408, L36
Nelson A. F., 2000, ApJ, 537, L65
Nelson A. F., 2006, MNRAS, 373, 1039
Offner S. S. R., Klein R. I., McKee C. F., 2008, ApJ, 686, 1174
Pickett B. K., Cassen P., Durisen R. H., Link R., 2000, ApJ, 529, 1034
Pickett M. K., Durisen R. H., 2007, ApJ, 654, L155
Rafikov R. R., 2005, ApJ, 621, L69
Rafikov R. R., 2007, ApJ, 662, 642
Shen S., Wadsley J., Hayfield T., Ellens N., 2010, MNRAS, 401, 727
Stadel J. G., 2001, PhD thesis, AA(UNIVERSITY OF WASHINGTON)
Stahler S. W., Palla F., 2005, The Formation of Stars
Stamatellos D., Hubber D. A., Whitworth A. P., 2007, MNRAS, 382, L30
Tobin J. J., Hartmann L., Chiang H., Looney L. W., 2010, ArXiv e-prints
Tohline J. E., 1982, Fundamentals of Cosmic Physics, 8, 1
Tomida K., Tomisaka K., Matsumoto T., Ohsuga K., Machida M. N., Saigo K., 2010, ApJ, 714, L58
Turner J. A., Chapman S. J., Bhattal A. S., Disney M. J., Pongracic H., Whitworth A. P., 1995, MNRAS, 277, 705
Vorobyov E. I., Basu S., 2007, MNRAS, 381, 1009
Vorobyov E. I., Basu S., 2010, ApJ, 714, L133
Wadsley J. W., Stadel J., Quinn T., 2004, New Astronomy, 9, 137
Walch S., Naab T., Burkert A., Whitworth A., Gritschneider M., 2009, ArXiv e-prints
Whitehouse S. C., Bate M. R., 2006, MNRAS, 367, 32
Whitworth A. P., Chapman S. J., Bhattal A. S., Disney M. J., Pongracic H., Turner J. A., 1995, MNRAS, 277, 727